

# Delocalized polaron and Burstein-Moss shift induced by Li in $\alpha$ -V<sub>2</sub>O<sub>5</sub>: DFT+DMFT study

Huu T. Do<sup>†,1,2</sup>, Alex Taekyung Lee<sup>†,1,2</sup>, Hyowon Park<sup>2,3</sup>, and Anh T. Ngo<sup>1,2,\*</sup>

<sup>1</sup>Department of Chemical Engineering, University of Illinois Chicago, IL 60607, USA.

<sup>2</sup>Materials Science Division, Argonne National Laboratory Argonne, IL 60439, USA.<sup>†</sup>

<sup>3</sup>Department of Physics, University of Illinois Chicago, IL 60607, USA.

(Dated: November 28, 2023)

We performed density functional theory (DFT)+*U* and dynamical mean field theory (DMFT) calculations with continuous time quantum Monte Carlo impurity solver to investigate the electronic properties of V<sub>2</sub>O<sub>5</sub> and Li<sub>*x*</sub>V<sub>2</sub>O<sub>5</sub> (*x* = 0.125 and 0.25). Pristine V<sub>2</sub>O<sub>5</sub> is a charge-transfer insulator with strong O *p*-V *d* hybridization, and exhibits a large band gap ( $E_{\text{gap}}$ ) as well as non-zero conduction band (CB) gap. We show that the band gap, the number of *d* electrons of vanadium,  $N_d$ , and conduction band (CB) gap for V<sub>2</sub>O<sub>5</sub> obtained from our DMFT calculations are in excellent agreement with the experimental values. While the DFT+*U* approach replicates the experimental band gap, it overestimates the value of  $N_d$  and underestimates the CB gap. In the presence of low Li doping, the electronic properties of V<sub>2</sub>O<sub>5</sub> are mainly driven by a polaronic mechanism, and electron spin resonance and electron nuclear double resonance spectroscopies observed the coexistence of free and bound polarons. Notably, our DMFT results identify both polaron types, with the bound polaron being energetically preferred, while DFT+*U* method only predicts the free polaron. Our DMFT analysis also reveals that increased Li doping leads to electron filling in the conduction band, shifting the Fermi level, this result consistent with the observed Burstein-Moss shift upon enhanced Li doping, and we thus demonstrate that the DFT+DMFT approach can be used for accurate and realistic description of strongly correlated materials.

## I. INTRODUCTION

Vanadium pentoxide (V<sub>2</sub>O<sub>5</sub>) is an interesting compound in the vanadium-oxide family, since its highest oxidation state +5 ( $d^0$ ) results in the strongest degree of an electronegativity and largest percentage of covalent bond in the oxide compounds, and it can be easily reduced to lower oxidation states [1, 2]. Furthermore, V<sub>2</sub>O<sub>5</sub> is a long attractive exemplar for both the fundamental research of electronic properties in transition oxides [3–6] and a variety of applications in photocatalysis, and smart window, especially in fabricating a cathode for electrochemical storage [7–12].

V<sub>2</sub>O<sub>5</sub> material exists in several polymorphs such as  $\alpha$ ,  $\beta$ ,  $\gamma'$  phases, [13, 14], and  $\alpha$  phase is the most stable at ambient conditions.  $\alpha$ -V<sub>2</sub>O<sub>5</sub> has a layered structure (Figure 1) with orthorhombic space group (*Pmmn*), and the layers interact with each other via a weak van der Waals force [15–17].  $\alpha$ -V<sub>2</sub>O<sub>5</sub> is a charge-transfer insulator, and it has band gap of 2.3–2.8 eV [7, 18–20]. There is also a gap in the conduction band (CB gap) around 0.5 eV separating between the split-off band and the main conduction band [6] (see Figure 2). The number of electrons in the V *d* manifold ( $N_d$ ) was also measured experimentally. Though V is in  $d^0$  state,  $N_d$  shows non-zero value due to the strong O *p*-V *d* hybridization. Resonant photoemission spectroscopy (RPES) estimated  $N_d = 2.0$  for V<sub>2</sub>O<sub>5</sub> [21], while cluster model predicted  $N_d = 1.2$  based on XPS and X-ray absorption spectroscopies (XAS) [22].

Previous DFT+*U* studies suggested the band gap of 1.5–2.2 eV, while the CB gap is only 0–0.15 eV [12, 23, 24]. This value is much smaller than the experimental value of 0.4–0.5 eV. Recent GW results showed that both band gap and CB gap

are increased to 2.4 eV and 0.3 eV, respectively. However, to our knowledge,  $N_d$  values are not reported in the past first-principles studies. Since the  $N_d$  represents the strength of the *p*-*d* hybridization and because V<sub>2</sub>O<sub>5</sub> is a charge-transfer insulator,  $N_d$  plays a crucial role in deciphering the electronic properties of V<sub>2</sub>O<sub>5</sub>.

Due to the layer-by-layer structure,  $\alpha$ -V<sub>2</sub>O<sub>5</sub> promises a potential candidate for the cathode material of Li-battery by intercalating Li<sup>+</sup> ions between layers, in particularly for rechargeable microbatteries due to very high specific densities and capacities [25, 26]. Depending on the Li ratio, several phases of Li<sub>*x*</sub>V<sub>2</sub>O<sub>5</sub> are observed:  $\alpha$  ( $x \leq 0.1$ ),  $\epsilon$  ( $0.33 \leq x \leq 0.64$ ), or  $\delta$  ( $0.7 \leq x \leq 1.0$ ) phases [27–29].

Li atoms in Li<sub>*x*</sub>V<sub>2</sub>O<sub>5</sub> donate electrons to V *d* bands and becomes Li<sup>+</sup> ions. With Li-doping, the electronic properties of  $\alpha$ -Li<sub>*x*</sub>V<sub>2</sub>O<sub>5</sub> are changed unexpectedly during the lithiation process. If the Li concentration is low ( $x = 0.001$  and  $0.005$ ), two types of polarons are observed experimentally: (i) free polarons localized at single V sites, and (ii) bound polarons delocalized over four V sites around a Li<sup>+</sup> ion [30, 31]. On the other hand, as *x* increases, the optical band gap is increased with Li doping, which indicates the Burstein-Moss shift, i.e., the Fermi level is shifted due to the doped electron in the conduction band [6].

There are several DFT+*U* studies of Li<sub>*x*</sub>V<sub>2</sub>O<sub>5</sub> in the literature, and they showed that the doped electron occupies the defect level located at the middle of the band gap, while the conduction band is empty [12, 23, 32, 33]. In these cases, the defect level or the electron is spatially localized on single V site, similar to the free polaron, with the migration barrier of 0.12–0.34 eV. [32, 33]. However, the bound polaron has not been found by DFT+*U* studies. In addition, since the electron occupies the defect level, there is no shift of the Fermi level within DFT+*U*.

In this work, we investigate the electronic structures of V<sub>2</sub>O<sub>5</sub> and Li<sub>*x*</sub>V<sub>2</sub>O<sub>5</sub> ( $x = 0.125$  and  $0.25$ ) using both DFT+*U* and

\* anhngo@uic.edu

<sup>†</sup> Huu T. Do and Alex Taekyung Lee contributed equally to this work.

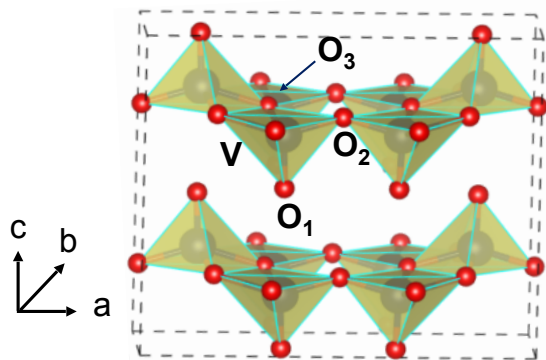


FIG. 1. Crystal structure of pristine  $\alpha$ - $V_2O_5$ , which includes two layers ( $1 \times 2 \times 1$  supercell).

DFT+DMFT methods. We show that  $N_d$  of  $V_2O_5$  within DFT+ $U$  approximates a twice of the experimental value, and  $N_d$  using DMFT method is similar to experimental value. We find that the bound polaron, where electron delocalized over four V sites, is energetically more stable than the free polaron within DMFT for  $Li_{0.125}V_2O_5$ . Moreover, we show that as  $x$  increases, the defect level is empty and electron occupies the conduction band within DMFT. This result is consistent with the Fermi level shift or Burstein-Moss effect in the experiments [6, 25].

We organize our manuscript as following. Sec. II describes in details the optimization of crystal structure and electronic calculations using DFT+ $U$  and DFT+DMFT. In the Sec. III, we show and discuss atomic structure and electronic properties of pure  $V_2O_5$  as well as their changes in  $Li_xV_2O_5$  ( $x = 0.125$  and  $0.25$ ). We conclude the content of our paper in the Sec. IV.

## II. COMPUTATIONAL DETAILS

### A. DFT+ $U$ and Structural Optimization

We performed density functional theory (DFT)+ $U$  calculations with a combination of the rotationally invariant formalism and the fully localized limit double-counting formula [34] implementing inside VASP package [35–37]. The projector augmented wave (PAW) method, which describes the relationship between core and valence electrons, was employed with the generalized gradient approximation (GGA) of Perdew-Burke-Ernzerhof (PBE) [38]. Since  $\alpha$ - $V_2O_5$  exhibits the layered structure (Figure 1), van der Waals correction (vdW), specifically DFT-D2 method [39, 40], was also applied to relax the structure.

For pristine and Li-doped  $V_2O_5$ , we adopted  $1 \times 2 \times 1$  and  $1 \times 2 \times 2$  supercells, that correspond to  $V_8O_{20}$  and  $V_{16}O_{40}$ , respectively. The Hubbard  $U$  parameter varied from 0 to 6 eV, while the Hund's coupling was fixed at  $J = 0$  eV. We utilized the kinetic energy cutoff of 600 eV, and  $3 \times 9 \times 4$  and  $3 \times 5 \times 3$   $k$ -point meshes for  $1 \times 2 \times 1$  and  $1 \times 2 \times 2$  supercells, respectively. The convergence of the structural relaxation was achieved once the atomic forces of all ions reached the value less than 0.01

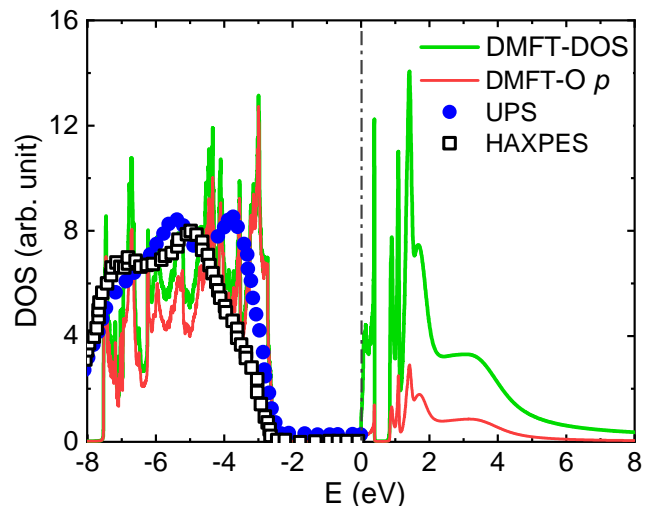


FIG. 2. DOS from experiments and DFT+DMFT. There is a gap in the conduction band (CB gap). We use ultraviolet photoemission spectroscopy (UPS) data with photon energies of 32 eV in Ref. [4], and hard X-ray photoemission spectroscopy (HAXPES) data in Ref. [12]. Here, all experiments were measured at room temperature. The parameters for DMFT calculation are set by  $U = 5.5$  eV,  $J = 0.5$  eV,  $\lambda = 0.4$  and  $T = 300$  K.

eV/Å.

We relaxed the lattice parameters of pristine  $\alpha$ - $V_2O_5$  using different  $U$  values with and without vdW correction, as summarized in Table I. The intercalating distance between two layers raises (parameter  $c$  along  $z$ -direction in Figure 1) with increasing  $U$ . Without vdW correction,  $c$  parameter increases from 4.729 to 4.790 Å with  $U = 0$  to 4 eV. With vdW correction,  $c$  parameter is suppressed from 4.427 to 4.469 Å with  $U = 0$  to 4 eV. We conclude that DFT+ $U$ (=4 eV)+vdW gives the best lattice parameters compared to the experimental value  $c = 4.392$  Å.

The lattice parameters of  $Li_{0.125}V_2O_5$  and  $Li_{0.25}V_2O_5$  are listed in Table II. The intercalating distance between two layers increases from 4.444 to 4.548 Å for  $x = 0.125$  and  $0.25$ , respectively. Similar to the pristine case, the DFT+ $U$ +vdW with  $U = 4$  eV gives the best match with the experiments. Since  $U = 4$  eV also provides a reasonable band gap for the pristine  $\alpha$ - $V_2O_5$

TABLE I. Lattice parameters of pristine  $\alpha$ - $V_2O_5$  using DFT+ $U$  and DFT+ $U$ +vdW, and experimental values.

$U$ (eV)	$a$ (Å)	$b$ (Å)	$c$ (Å)	$V$ (Å) <sup>3</sup>
0	11.558	3.562	4.729	194.706
3	11.495	3.636	4.790	199.242
4	11.485	3.636	4.790	199.901
0+vdW	11.634	3.532	4.427	181.919
3+vdW	11.563	3.588	4.460	185.030
<b>4+vdW</b>	<b>11.548</b>	<b>3.606</b>	<b>4.469</b>	<b>186.127</b>
Exp. <sup>a</sup>	11.548	3.577	4.392	181.454

<sup>a</sup> Experimental values are taken and averaged from X-ray data in Ref. [13, 14].

TABLE II. Lattice parameters of  $\text{Li}_{0.125}\text{V}_2\text{O}_5$  and  $\text{Li}_{0.25}\text{V}_2\text{O}_5$  using DFT+ $U$  and DFT+ $U$ +vdW, and experimental data. We relax the structures using  $1 \times 2 \times 1$  and  $1 \times 2 \times 2$  supercells, the values for the  $1 \times 1 \times 1$  unit cell are shown.

$x$	$U$ (eV)	$a$ (Å)	$b$ (Å)	$c$ (Å)	$V$ (Å) <sup>3</sup>
	0	11.498	3.564	4.742	194.322
	4	11.545	3.635	4.632	194.387
0.125	0+vdW	11.562	3.534	4.453	181.941
	<b>4+vdW</b>	<b>11.565</b>	<b>3.604</b>	<b>4.444</b>	<b>185.227</b>
	Exp. <sup>a</sup>	11.470	3.570	4.470	183.037
0.25	0+vdW	11.521	3.538	4.444	181.12
	<b>4+vdW</b>	<b>11.514</b>	<b>3.552</b>	<b>4.548</b>	<b>185.980</b>
	Exp. <sup>b</sup>	11.410	3.570	4.540	184.931

<sup>a</sup> Experimental values are taken and averaged from X-ray data in Ref. [28, 41]

<sup>b</sup> Similar references to  $x = 0.125$  case<sup>a</sup>

(Figs. 3 and 4), hereafter we focus on the structure obtained using  $U = 4$  eV within DFT+ $U$ +vdW, unless specified.

## B. DFT+DMFT method

At the first step of a conventional DFT+DMFT procedure [42–44], we employ DFT+ $U$ +vdW to optimize atomic structures and subsequently create localized Wannier orbitals. For pristine  $\text{V}_2\text{O}_5$ , we use  $U = 4$  eV, as mentioned previously. On the other hand, in Li-doped  $\text{V}_2\text{O}_5$ , the addition of electrons to the system leads to the emergence of two types of polarons [30, 31], which result in distinct local structural distortions. However, the optimized structure obtained using  $U = 4$  eV only provides the free polaron, where the electron is localized at a single V site, and significant structural relaxation is confined to the vicinity of this electron-localized V site. Therefore, to capture the structural distortion induced by the delocalized (or bound) polaron, we also relax the structure with  $U = 0$  eV, while maintaining fixed lattice parameters. By examining these two different structures, we can compare the two types of polarons within both DFT+ $U$  and DFT+DMFT. Further details can be found in Appendix C.

In the second step of DFT+DMFT calculations,  $V d$  and  $O p$  orbitals were constructed to represent a hybridization subspace by projecting the Kohn-Sham (KS) plane-wave functions onto maximally localized Wannier functions (MLWFs) [45]. In this step, non-spin polarized DFT ( $U = 0$  eV) scheme is used. In the last step,  $V d$  manifolds were implemented by using the continuous time quantum Monte Carlo (CTQMC) impurity solver within DMFT [42, 46, 47]. An additional unitary rotation transformation for the Wannier subspace of  $V d$  orbitals was applied to minimize the off-diagonal hopping terms [42]. In these systems, we consider the hybridized region within energy window of 10 eV around the Fermi level [see Fig. 10 in Appendix A].

The rotationally invariant Coulomb interaction in the form

of the Slater-Kanamori interaction Hamiltonian [48–50] is

$$\hat{H}_{\text{SK}} = U \sum_{\alpha} \hat{n}_{\alpha\uparrow} \hat{n}_{\alpha\downarrow} + \frac{1}{2} \sum_{\alpha \neq \beta} \sum_{\sigma \sigma'} (U' - J \delta_{\sigma \sigma'}) \hat{n}_{\alpha\sigma} \hat{n}_{\beta\sigma'} - \sum_{\alpha \neq \beta} \left( J c_{\alpha\uparrow}^{\dagger} c_{\alpha\downarrow} c_{\beta\downarrow}^{\dagger} c_{\beta\uparrow} + J' c_{\beta\uparrow}^{\dagger} c_{\beta\downarrow}^{\dagger} c_{\alpha\uparrow} c_{\alpha\downarrow} \right). \quad (1)$$

Here,  $c_{\sigma}$  and  $c_{\sigma}^{\dagger}$  denote the fermion annihilation and creation operators, where  $\sigma$  is spin.  $U$  denotes intra-orbital density-density interaction parameter,  $U'$  is inter-orbital density-density interaction parameter,  $J$  is spin-flip interaction parameter, and  $J'$  is pair-hopping interaction parameter.  $U' = U - 2J$ ,  $J' = J$  are due to the rotational invariance.

To investigate the temperature effect, we employed electronic temperatures of 300 K. This choice is motivated by the application of  $\text{V}_2\text{O}_5$  as a cathode material for batteries, which typically operate at room temperature. For the single Li-doped  $\text{V}_2\text{O}_5$ , we also considered 150 K and found the electronic structures to be nearly indistinguishable. It is worth noting that within the CTQMC framework, we limited our considerations to density-density interactions. Given that there are 16 vanadium atoms in the supercell, a full Coulomb interaction calculation would be computationally demanding.

In the DMFT self-consistent calculations, the convergence of self-energy is determined once local or lattice self-energy  $\Sigma^{\text{loc}}(i\omega_n)$  approaches the impurity self-energy  $\Sigma^{\text{imp}}(i\omega_n)$ , with the discrete Matsubara frequency  $\omega_n$  [46, 51]. {Note that the self-energy is approximated as a local quantity in the correlated subspace, i.e.,  $\Sigma(\mathbf{k}, i\omega_n) \simeq \Sigma(i\omega_n)$  [46].} So, the total DFT+DMFT energy is given by:

$$E^{\text{TOT}} = E^{\text{DFT}}(\rho) + \sum_{m, \mathbf{k}} \epsilon_m(\mathbf{k}) \cdot [n_{mm}(\mathbf{k}) - f_m(\mathbf{k})] + E^{\text{POT}} - E^{\text{DC}}, \quad (2)$$

where  $E^{\text{DFT}}$  is the DFT energy computed by the electronic charge density  $\rho$ .  $\epsilon_m(\mathbf{k})$  denotes as the DFT eigenvalues, and  $n_{mm}(\mathbf{k})$  and  $f_m(\mathbf{k})$  are the diagonal DMFT occupancy matrix element and Fermi function, respectively, with the KS band  $m$  and momentum  $\mathbf{k}$ . The potential energy  $E^{\text{POT}}$  is calculated by using Migdal-Galiski formula: [52]:

$$E^{\text{POT}} = \frac{1}{2} \sum_{\omega_n} [\Sigma^{\text{loc}}(i\omega_n) \cdot G^{\text{loc}}(i\omega_n)]. \quad (3)$$

Here, the local Green's function is simplified by  $G^{\text{loc}}(i\omega_n) = \sum_{\mathbf{k}} G^{\text{loc}}(\mathbf{k}, i\omega_n)$  [46, 51].

Similar to the conventional fully localized limit, we used a double counting energy  $E^{\text{DC}}$  [43, 44, 51] to consider to the double counting corrections for DFT+DMFT calculation as:

$$E^{\text{DC}} = \frac{(U - \lambda)}{2} N_d \cdot (N_d - 1) - \frac{J}{4} N_d \cdot (N_d - 2), \quad (4)$$

where  $N_d$  is called the formal  $d$ -electron number obtained self-consistently at each  $V d$  site, and  $\lambda$  is the double counting parameter [44].  $N_d$  is directly computed from the local Green function  $G^{\text{loc}}(\mathbf{k}, \mathbf{k}', i\omega_n)$ :

$$N_d = \sum_{a, n} \sum_{\mathbf{k}, \mathbf{k}'} \text{Im} \{ [\phi_a^a(\mathbf{k})]^* G^{\text{loc}}(\mathbf{k}, \mathbf{k}', i\omega_n) \phi_a^a(\mathbf{k}') \}. \quad (5)$$

Here, the  $\omega_n$  is the Matsubara frequency, and  $\phi_d^a(\mathbf{k})$  represents the normalized  $d$ -orbital wave-function, which is transformed from  $\phi_d^a(\mathbf{r})$  with the real coordinates  $\mathbf{r}$  positioning on a transition metal ion [53]. The spectral function or density of state (DOS) is calculated by using the maximum entropy method [54]:

$$A(\omega_n) = -\frac{1}{\pi} \text{Im} \left[ \sum_{\mathbf{k}} G^{\text{loc}}(\mathbf{k}, \omega_n) \right]. \quad (6)$$

### III. RESULTS AND DISCUSSION

#### A. Pristine $\alpha$ -V<sub>2</sub>O<sub>5</sub>

As mentioned,  $\alpha$ -V<sub>2</sub>O<sub>5</sub> has layered structure with van der Waal interaction between the layers. A vanadium atom stands at a distorted pyramidal coordination surrounding by five oxygen atoms which are classified into three different types, as depicted in Figure 1: (i) vanadyl oxygen (O<sub>1</sub> forms a double bond with the vanadium atom), (ii) bridge oxygen (O<sub>2</sub> connects two vanadium atoms in different chain) and (iii) chain oxygen (O<sub>3</sub> bonds to three vanadium atoms) [3, 55].

V has 5+ charge state with  $d^0$  in V<sub>2</sub>O<sub>5</sub>, and thus the conduction bands are largely dominated by V  $d$  bands, whereas the valence bands near the Fermi level are significantly from O  $p$  bands (Figures 2 and 3). From the structure of V-O bonds, V  $d_{x^2-y^2}$  and  $d_{z^2}$  forms  $\sigma$  bonds  $p$  orbitals of O<sub>1</sub> and O<sub>2</sub>+O<sub>3</sub> atoms, respectively, while  $t_{2g}$  orbitals forms  $\pi$  bonds with O atoms. Since one of the apical oxygen is missing compared to the VO<sub>6</sub> octahedron, the cubic symmetry of  $d$  bands is broken. Thus, doubly degenerate  $e_g$  bands split into  $d_{x^2-y^2}$  and  $d_{z^2}$  bands, and  $t_{2g}$  bands break into  $d_{xy}$  band as well as double degeneracy of  $d_{xz}+d_{yz}$  bands, as presented in Figure 3. As a result, there is splitting in the V  $d$  states in the conduction band, as presented in Figure 3. The lower band called as "split-off band", and the higher band is named as "main conduction band".

We first study the effect of  $U$  on the width of the energy gap ( $E_{\text{gap}}$ ), and the CB gap (due to separating between the split-off band and the main conduction band) using DFT+ $U$ , as illustrated in Figure 4(a). At  $U = 0$  eV,  $E_{\text{gap}} = 1.7$  eV is much smaller than the experimental values of 2.3–2.8 eV [7, 18, 19]. The CB gap of 0.4 eV is comparable to the experimental splitting 0.5 eV [6, 56]. At  $U = 4$  eV,  $E_{\text{gap}} = 2.3$  eV agrees well with prior DFT+ $U$  studies [13, 22] and the experiments. However, the CB gap is only 0.20 eV, which is narrower than the experimental result [6, 56]. Therefore, we remark that  $E_{\text{gap}}$  ascends with respect to  $U$ , whereas the CB splitting width descends versus  $U$ .

In Fig. 4(b), we observe that DFT+ $U$  overestimates the number of  $d$  electron ( $N_d$ ) in V. This value is around 3.8–4.0 in the  $U$  range of 0–6 eV, but larger than the experimental ones such as  $N_d = 2.0$  measured by RPES [21], and 1.2 calculated by the cluster model based on XPS and XAS [22]. Therefore, DFT+ $U$  has a critical limitation to describe the physics of V  $d$  bands. We also note that the  $N_d$  value depends on the projection methods. At  $U = 0$  eV,  $N_d$  using the Wannier projectors

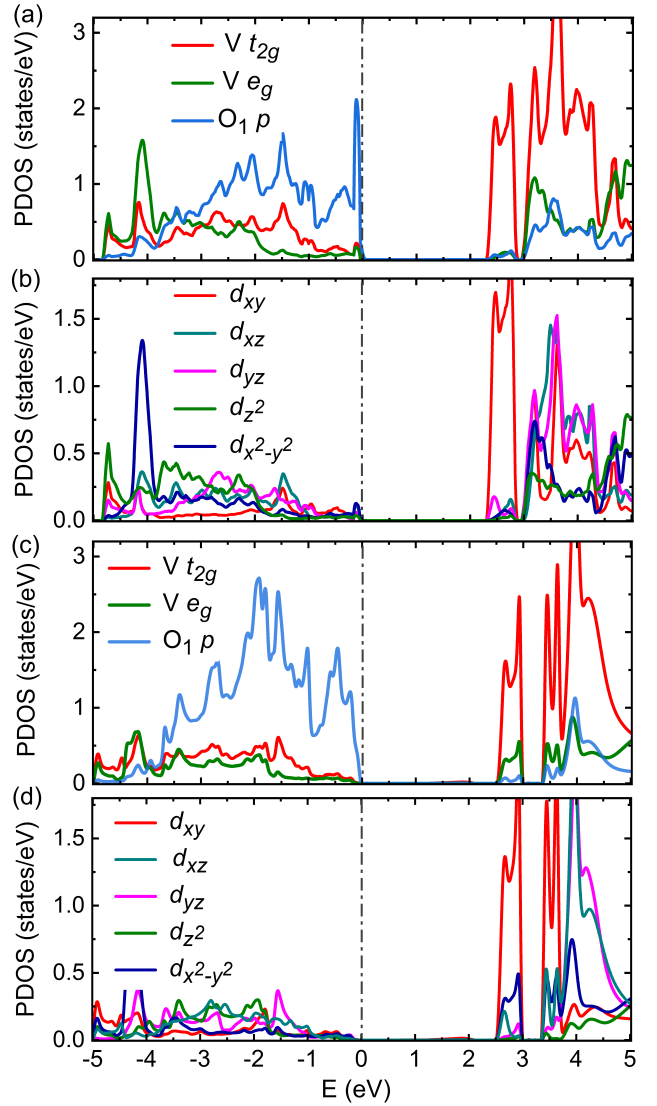


FIG. 3. Projected density of states onto V  $d$  and O  $p$  of pristine V<sub>2</sub>O<sub>5</sub>, using (a)-(b) DFT+ $U$  with  $U = 4$  eV and  $J = 0$  eV, and (c)-(d) using DFT+DMFT with  $U = 5.5$  eV,  $J = 0.5$  eV.  $\lambda = 0.4$  and temperature  $T = 300$  K are used. Valence band maximum (VBM) is set to be zero.

gets 2.64 [corresponds to DMFT with  $U = 0$  in Figure 4(b)], and it is smaller than  $N_d = 4.0$  from the PAW projectors.

In order to resolve the limitation of DFT+ $U$ , we performed DFT+DMFT calculations for pristine  $\alpha$ -V<sub>2</sub>O<sub>5</sub>. First, we compute  $E_{\text{gap}}$  as a function of  $U$  without the double counting parameter (i.e.,  $\lambda = 0$ ), [Figure 4(a)]. At  $\lambda = 0$ ,  $E_{\text{gap}}$  is 1.71–1.95 eV with  $U = 2.5$ –6.5 eV and less sensitive on  $U$  in comparison with DFT+ $U$ , and it does not approach the experimental value of 2.3–2.8 eV [7, 18, 19]. Since V<sub>2</sub>O<sub>5</sub> exhibits as a charge-transfer insulating system, the  $p$ - $d$  hybridization is more important than the  $d$ - $d$  correlation for determining its band gap. The double counting correction  $\lambda$  controls the degree of  $p$ - $d$  covalency, increasing this parameter results in larger separation between O  $p$  and V  $d$  bands and thus enlarges  $E_{\text{gap}}$ . At  $\lambda = 0.4$ , we obtain  $E_{\text{gap}} = 2.35$ –2.55 eV for  $U$

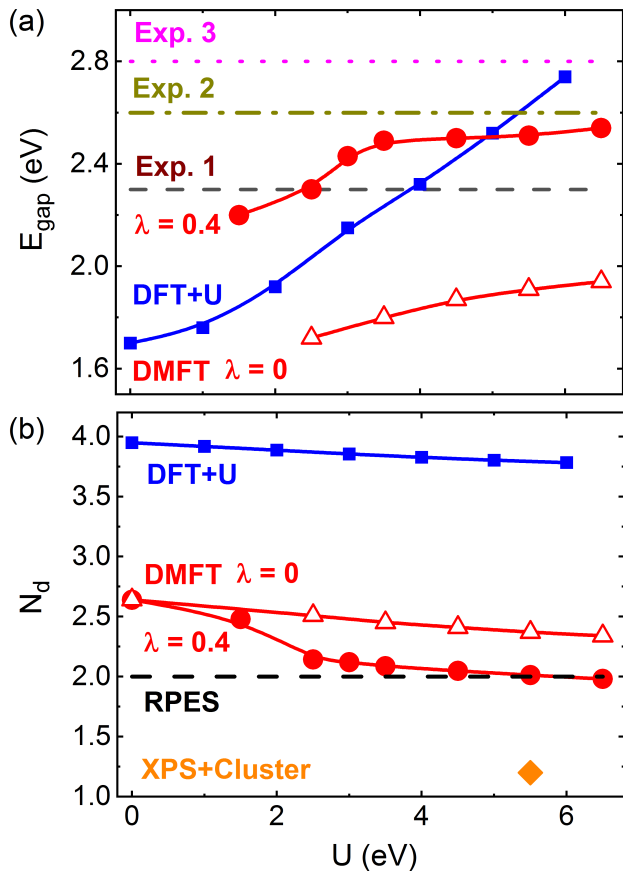


FIG. 4. (a) Energy gap ( $E_{\text{gap}}$ ) of pristine  $\text{V}_2\text{O}_5$  as a function of  $U$ . The experimental values of the band gap are taken from Ref. [18] (Exp. 1, black dashed line), Ref. [19] (Exp. 2, dark yellow dashed dotted line) and Ref. [7] (Exp. 3, magenta dotted line). (b) the number of  $d$  electron ( $N_d$ ) of V atom in  $\text{V}_2\text{O}_5$ , as a function of  $U$ . Data of RPES and cluster model are from Ref. [21] and Ref. [22], respectively.  $J = 0$  is used for DFT+U, and  $J = 0.5$  eV and  $T = 300$  K are used for DMFT calculations. Two different values of the double counting parameter are shown:  $\lambda = 0$  and  $0.4$ .

values of 2.0–6.5 eV, which are in very good agreement to the experimental values.

Nonzero  $\lambda$  is also needed for the reasonable  $N_d$ , as depicted in Figure 4(b). The  $N_d$  values using  $\lambda = 0$  with  $U = 1.5$ –6.5 eV are 2.50–2.34, always larger than the experimental values [21, 22, 57]. If  $\lambda = 0.4$  is implemented, we show  $N_d = 2.50$ –1.98 with the range of  $U$  from 2.5 to 6.5 eV. Particularly,  $N_d = 2.01$  for  $U = 5.5$  eV matches well with the RPES value [21]. Therefore, combining the results of  $E_{\text{gap}}$  and  $N_d$ , we conclude that  $U = 5.5$  eV and  $\lambda = 0.4$  are the best parameters for DMFT computations, with  $E_{\text{gap}} = 2.52$  eV and  $N_d = 2.01$ .

Different from our DMFT calculation and the previous RPES measurement ( $N_d = 2.0$ ) [21], Mossaneck *et al.* showed  $N_d \sim 1.2$  from the single impurity cluster model, solved by configuration interaction method [22]. They considered  $[\text{VO}_5]^{-5}$  ( $\text{V}^{5+}$ ) with  $C_{4v}$  symmetry, corresponds to the square base pyramid structure. In order to explain the difference of  $N_d$  between our DMFT and the cluster model, we calculate

TABLE III. Contribution of  $3d^n L^n$  states to the ground state of  $\text{V}_2\text{O}_5$ .

Configuration	DMFT	cluster [22]
$3d^0$	2%	20%
$3d^1 L$	22%	47%
$3d^2 L^2$	41%	28%
$3d^3 L^3$	25%	N/A

the contribution of  $d^n L^n$  configurations to the ground state of  $\alpha$ - $\text{V}_2\text{O}_5$ , as summarized in Table III. The weight of  $d^0$  is only 2% within DMFT, whereas it is 20% from the cluster model [22]. From our DMFT calculations,  $3d^2 L^2$  configuration has the largest weight of 41%, and  $3d^1 L^1$  and  $3d^3 L^3$  account for 22% and 25% of population probabilities, respectively. Within the cluster model,  $3d^1 L^1$  contributes the largest probability of 47%, and the weight of  $3d^2 L^2$  configuration is 28% [22]. We note that the single impurity cluster model does not include the hybridization between clusters, i.e., there are no V-V nor O-O interactions, and therefore both  $d$  and  $p$  state do not have dispersion. The absence of the band dispersion in their model may give rise to the suppression of  $N_d$ .

Spectral functions, i.e., DOS from DMFT calculations using  $U = 5.5$  eV and  $\lambda = 0.4$  are presented in Figures 3(c) and (d). The CB gap of 0.4 eV between the split-off band and the main conduction band is close to the experimental value 0.5 eV from the photoluminescence measurements [6, 56]. We emphasize that while DFT+U only provides reasonable value of  $E_{\text{gap}}$ , experimental values of  $E_{\text{gap}}$ ,  $N_d$  and CB gap are successfully reproduced by our DMFT calculations. That implies the accurate method for the electron correlation is essential, even for  $d^0$  band systems. Similar to DFT+U, the split-off band is mainly from  $d_{xy}$  band within DMFT. The O  $p$  character is dominant near the valence band maximum, especially between  $-3.5$  to  $-2.0$  eV [Figure 3(c)]. In figure 2, we also show that our DMFT DOS are well matched to UPS [58] and HAXPES [12] experiments, particularly at the positions of the Fermi level and the range of valence band.

## B. $\alpha$ - $\text{Li}_x\text{V}_2\text{O}_5$ ( $x = 0.125$ and $0.25$ )

In this section, we consider Li-doped  $\alpha$ - $\text{V}_2\text{O}_5$ , including  $\alpha$ - $\text{Li}_{0.125}\text{V}_2\text{O}_5$  and  $\alpha$ - $\text{Li}_{0.25}\text{V}_2\text{O}_5$ , using both DFT+U and DMFT methods.

### 1. $\alpha$ - $\text{Li}_{0.125}\text{V}_2\text{O}_5$

$\alpha$ - $\text{Li}_{0.125}\text{V}_2\text{O}_5$  is formed by intercalating one Li atom in the  $1 \times 2 \times 2$  supercell (corresponds to  $\text{Li}_1\text{V}_{16}\text{O}_{40}$ ). The distance between Li ion and another one in the next supercell is 11.55 Å, 7.21 Å, and 8.94 Å along  $a$ ,  $b$ ,  $c$  directions, respectively. Thus, we assume that the interaction between Li defects are almost negligible once the periodic boundary condition is implemented. We examined several initial different positions of doping single Li ion (see Appendix B), and found that the

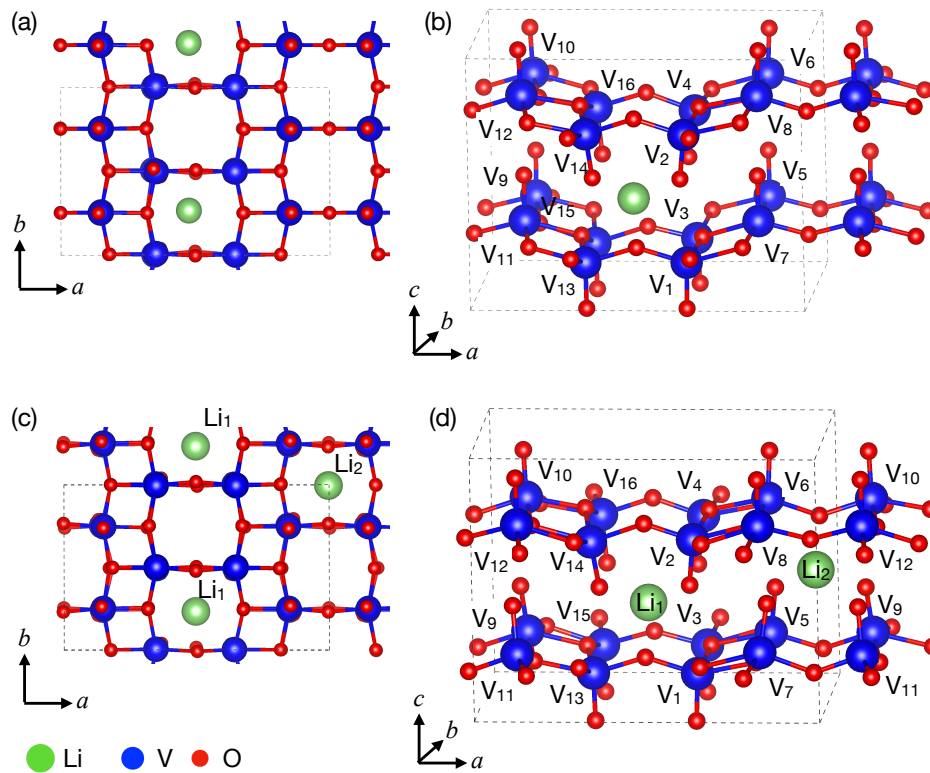


FIG. 5. Atomic structure of (a)-(b)  $\text{Li}_{0.125}\text{V}_2\text{O}_5$  and (c)-(d)  $\text{Li}_{0.25}\text{V}_2\text{O}_5$ . Indices of V atoms are shown.

TABLE IV. Magnetic moments ( $\mu_B$ ) of V atoms in  $\alpha\text{-Li}_x\text{V}_2\text{O}_5$  ( $x = 0.125$  and  $0.25$ ), within DFT+ $U$  calculations.  $U = 4$  eV and  $J = 0$  are used. Indices of V atoms are shown in Figure 5.

$x =$	V <sub>1</sub>	V <sub>2</sub>	V <sub>3</sub>	V <sub>7</sub>	V <sub>11</sub>	V <sub>13</sub>	V <sub>14</sub>	V <sub>15</sub>	other V
0.125	0.01	0.00	0.08	0.00	0.00	0.01	0.02	1.11	0.00
0.25	0.00	0.13	0.00	1.08	0.12	0.00	1.08	0.00	0.00

most stable position of Li ion is middle of a hole, as depicted in Figure 5(a). Li atom gets closer to the lower layer than the upper layer [Fig. 5(b)]. Distances from Li ion to the lower and upper V layers are 3.506 and 5.381 Å, respectively. The stable position of Li ion is similar to structure obtained in the previous DFT+ $U$  studies [12, 23].

Once Li atoms are doped, they donate one electron per Li ion to  $\text{V}_2\text{O}_5$  system, and become  $\text{Li}^+$ . Li  $s$  bands are fully empty and far above the Fermi level by 6.5 eV, indicating  $\text{Li}^+$ . Within DFT+ $U$ , the splitting between the split-off band and the main CB becomes even smaller for  $\text{Li}_{0.125}\text{V}_2\text{O}_5$ , and the CB gap is nearly zero, while the CB gap is 0.1 eV for pristine  $\alpha\text{-V}_2\text{O}_5$  within DFT+ $U$  (Figure 6).

DFT+ $U$  results point out a defect level is created at middle of the band gap for doping a single Li-ion in  $\text{V}_2\text{O}_5$  framework [Figs. 6(a)-(b)]. The defect band occupies one electron, spin-up defect level is filled and located at 0.62 eV above VBM, while spin-down level is empty. The position of the spin-up defect level is similar to the previous DFT+ $U$  ( $=4$  eV) study of

$\alpha\text{-Li}_{0.028}\text{V}_2\text{O}_5$  (correspond to  $\text{Li}_1\text{V}_{72}\text{O}_{180}$ ), where Li defect level is near VBM+1.0 eV [23].

The origin of the defect level is the charge disproportionation of the V atoms, since the electron occupying the defect level spatially localizes on single V atom. Given that only spin-up defect band is occupied, magnetic moments of V atoms shown in Table IV directly indicates the charge disproportionation in Li-doped  $\text{V}_2\text{O}_5$  within DFT+ $U$ . Specifically, one electron from Li is donated at V<sub>15</sub> atom, which is the nearest neighbor of Li atom with distance of 3.075 Å (see Figure 5).

The localization of the electron induces a polaronic effect in  $\text{Li}_x\text{V}_2\text{O}_5$  [12, 30, 31, 59]. The ESR and ENDOR spectroscopies, and electronic conductivity measurement proposed two types of charge carriers in  $\text{Li}_{0.005}\text{V}_2\text{O}_5$  [31] and  $\text{Li}_{0.001}\text{V}_2\text{O}_5$  [30]: (i) free polarons localized at single vanadium sites, and (ii) bound polarons delocalized over four vanadium sites around a  $\text{Li}^+$  ion (see Fig. 8 for schematic illustrations). Since the electron prefers to occupy a single V, this corresponds the free polaron [Fig. 8(a)]. According to previous DFT+ $U$  studies, the electron could be positioned on other V sites with higher value than the ground state by 0.1–0.2 eV [32]. The migration barrier from DFT+ $U$  calculations are 0.12–0.34 eV [32, 33], close to the experimental values 0.27–0.28 eV [59, 60]. However, the bound polaron has not been observed by DFT+ $U$  calculations.

To explore the polaronic effect suggested in the previous experiments [30, 31], we performed DFT+DMFT calculations using parameters analogous to those of pristine  $\text{V}_2\text{O}_5$  ( $U = 5.5$

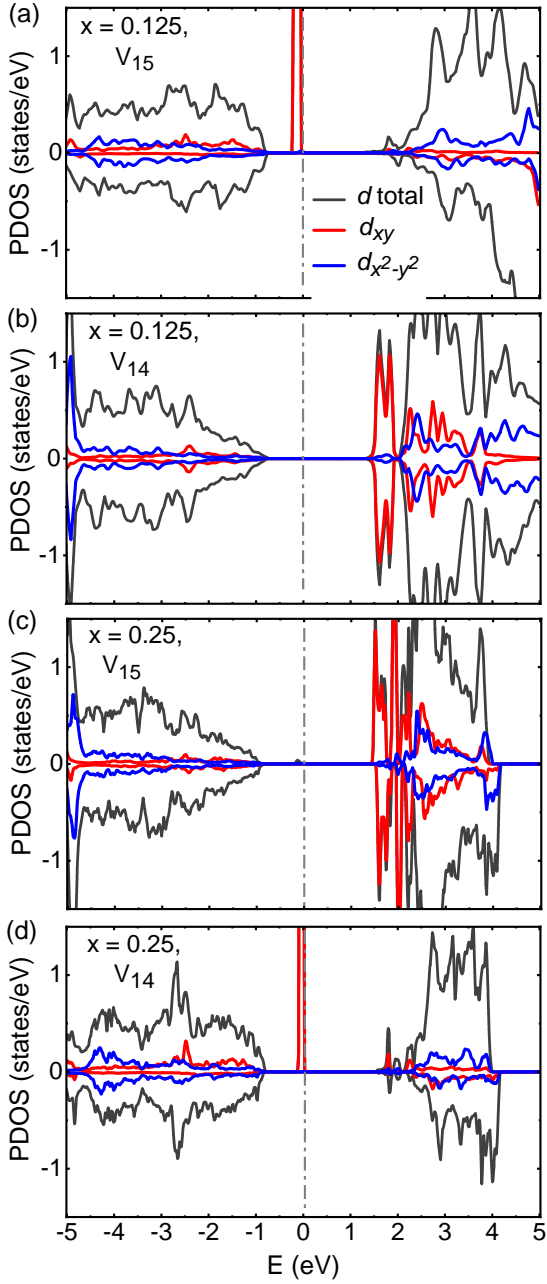


FIG. 6. DOS and projected density of states (PDOS) onto V  $d$  orbital for (a)-(b)  $\alpha$ - $\text{Li}_{0.125}\text{V}_2\text{O}_5$  and (c)-(d)  $\alpha$ - $\text{Li}_{0.25}\text{V}_2\text{O}_5$ , using DFT+ $U$ .  $U = 4$  eV and  $J = 0$  eV are used. Fermi energy is set to be zero.

eV,  $J = 0.5$  eV and  $\lambda = 0.4$  at  $T = 300$  K). We examine two different types of structural distortions, as stated in Sec. II B. By considering two different structures, we aim to disentangle the effect of structural distortion and electron correlation on the electron distribution. Surprisingly, as shown in Table V, the bound polaron is more stable than the free polaron within DMFT, while the energy difference is only 0.11 eV. We emphasize that the experiments observed simultaneously both types of polarons [30, 31, 59], which are fruitfully interpreted by smaller energy difference between the two states within

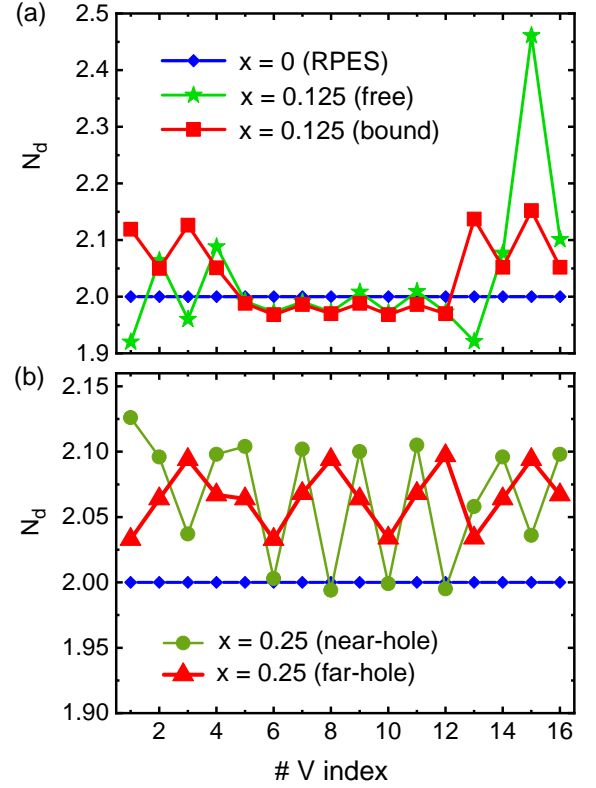


FIG. 7.  $N_d$  of V atoms in  $\text{Li}_x\text{V}_2\text{O}_5$  for (a)  $x = 0.125$  (b)  $x = 0.25$ . The  $N_d$  value is calculated by DFT+DMFT method with  $U = 5.5$  eV,  $J = 0.5$  eV,  $\lambda = 0.4$  at  $T = 300$  K. We consider  $\text{Li}^+$  ion is the center of system, we classify the  $N_d$  values into high  $N_d$  value for nearest V atom, medium value for next-nearest and low value for far V atoms [see Fig. 5]. Blue diamond with line show the background homogeneous  $N_d$  of V atom in our pristine  $\text{V}_2\text{O}_5$  and RPES measurement [21]. For which V atoms have  $N_d > 2.0$  will receive a electron donated by Li atom.

our DFT+DMFT results (Table V). Furthermore, both states can also explain the diminishing effect of  $d_{xy}$  (or  $d_{xy}$  occupation) and inhomogeneous electron distribution by scanning transmission X-ray microscopy (STXM) in Li-doped  $\text{V}_2\text{O}_5$  [12, 25].

For the free polaron within DFT+DMFT, the doped electron predominantly occupies the  $\text{V}_{15}$  site, similar to DFT+ $U$ . The electron gain of  $\text{V}_{15}$  is 0.46  $e$ , while  $N_d$  for  $\text{V}_2$ ,  $\text{V}_4$ ,  $\text{V}_{14}$ , and  $\text{V}_{16}$  exhibit a slight increase, ranging from 0.05 to 0.08  $e$  [see

TABLE V. Energy difference between free and bound polarons calculated within DFT+ $U$  and DMFT for  $\text{Li}_{0.125}\text{V}_2\text{O}_5$ . Here, we used spin-polarized DFT+ $U$  with  $U = 4$  eV and  $J = 0$  eV. The parameters for DMFT are  $U = 5.5$  eV and  $J = 0.5$  eV,  $\lambda = 0.4$  at room temperature. We set the energy level of the free polaron at 0 eV and compare with bound one.

Methods	free polaron	bound polaron
DFT+ $U$	0	0.51 eV
DMFT	0	-0.11 eV

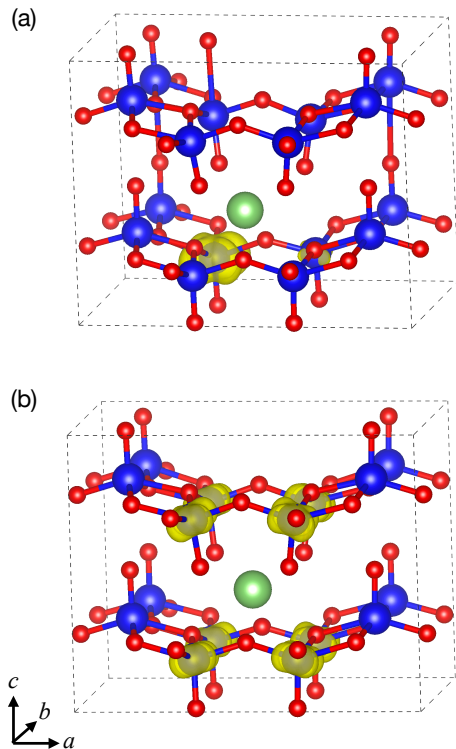


FIG. 8. Schematic illustration of (a) free and (b) bound polarons in  $\text{Li}_{0.125}\text{V}_2\text{O}_5$ . The atomic positions are referred to Fig. 5(b).

Fig. 7(a)]. The bound polaron depicted by DFT+DMFT is notably intriguing. This state has no defect level in the band gap and is hidden above the CBM [Figs. 9(a)–(c)]. The electron at the Li defect level is thus empty, and doped electrons are occupying the V  $d_{xy}$  state of the split-off band. V ions at the lower layer ( $V_1, V_3, V_{13},$  and  $V_{15}$ ) gain the largest amount of electron around  $0.12\text{--}0.16 e$  per V atom [Figure 9(a)], while the upper-layer V ions ( $V_2, V_4, V_{14},$  and  $V_{16}$ ) also increase about  $0.05 e$  [Figure 9(b)]. On the other hand, the other V ions far from Li ion lose  $0.03 e$  per V atom, and their  $d$  bands are empty [Figure 9(c)]. Our DMFT result indicates that the electron localizing in V ions close to Li site, consistent with the experiments [30, 31].

To understand the reason why we cannot observe the bound polaron by DFT+ $U$  with full atomic relaxation, we carried our a simple test by taking the bound polaron structure within DMFT calculation and then adopting the spin-polarized DFT+ $U$ (=4 eV)+vdW. As presented in Table V, the total energy of the bound polaron is higher than the free one by 0.51 eV, indicating that bound polaron is unstable within DFT+ $U$ . Our results suggest that electron localization in  $\text{V}_2\text{O}_5$  is overestimated within DFT+ $U$ , and the discrepancy is rectified by DFT+DMFT.

Another important feature from our DMFT results is nonzero CB gap of 0.4 eV for  $\text{Li}_{0.125}\text{V}_2\text{O}_5$ , as depicted in Figures 9(a)–(c). Recent photoluminescence, optical absorption, and photoemission spectroscopy suggested that CB gap is 0.5 eV for  $\text{Li}_x\text{V}_2\text{O}_5$  ( $0 \leq x \leq 1$ ) [6]. Therefore, while DFT+ $U$

fails to obtain nonzero CB gap for Li-doped  $\text{V}_2\text{O}_5$ , the splitting of the split-off band and the main CB gap is successfully described by DMFT.

## 2. $\alpha\text{-Li}_{0.25}\text{V}_2\text{O}_5$

We now consider  $\text{Li}_{0.25}\text{V}_2\text{O}_5$  by adding two Li atom in the  $1 \times 2 \times 2$  supercell (the stoichiometric formula is  $\text{Li}_2\text{V}_{16}\text{O}_{40}$ ). From the experiment,  $\alpha$  and  $\epsilon$  phases are coexistent for  $x = 0.25$  [27–29], but we only consider  $\alpha\text{-Li}_{0.25}\text{V}_2\text{O}_5$ . As shown in Figure 5, we choose two Li ions positioned at two of four large holes: (i) *near-hole* with Li-Li distance ( $d_{\text{Li-Li}}$ ) of 3.166 Å, and (ii) *far-hole* with  $d_{\text{Li-Li}} = 8.104$  Å. The far-hole configuration is more stable than the near-hole structure by 0.19 eV because the Coulomb interaction between  $\text{Li}^+$  ions becomes weaker. Hereafter we only focus on the far-hole configuration.

The electronic properties of  $x = 0.25$  case behave relatively similar to the  $x = 0.125$  one. Within DFT+ $U$ , the electron or free polaron is strongly localized at the defect level, i.e., two doped electrons are trapped on  $V_7$  and  $V_{14}$  [Table IV and figures 6(c)–(d)]. Therefore, the spin-up defect levels are almost degenerate near 0.62 eV above VBM and [Figure 6(c)].

The bound polaronic state in  $x = 0.25$  by DFT+DMFT shows that the electron is more delocalized than  $x = 0.125$ . As presented in figures 7(b) and 9(d)–(f),  $d$  bands of all V atoms gain electron and partially occupy, so the distribution of doped electrons in  $\text{Li}_{0.25}\text{V}_2\text{O}_5$  become more homogeneous than  $\text{Li}_{0.125}\text{V}_2\text{O}_5$ . No the defect level is occurred in the band gap, and electrons are occupied V  $d_{xy}$  bands, which results in the metallic state compared with the prediction of insulating case by DFT+ $U$ .

When  $x$  is increased from 0.125 to 0.25, the Fermi level within DMFT is increased since the additional electrons are occupying the lowest conduction band ( $d_{xy}$ ), while the electrons are occupying the mid-gap defect state and thus the Fermi level is unchanged within DFT+ $U$ . As shown in Figures 4 and 9, the Fermi level from DMFT with respect to the valence band maximum (VBM) is increased from 2.52 to 2.83 eV for  $x = 0$  to 0.25. Indeed, the photoluminescence, optical absorption and depth-resolved cathodoluminescence spectroscopies suggested the occurrence of the Burstein-Moss effect in Li-doped  $\text{V}_2\text{O}_5$  [6, 25, 41], consistent with our DMFT results.

## IV. CONCLUSION

Based on the DFT+ $U$  and DFT+DMFT study, we have shown that the precise description of the electron correlation is important on the electronic structure of  $\text{V}_2\text{O}_5$  and  $\text{Li}_x\text{V}_2\text{O}_5$  ( $x = 0.125$  and 0.25). For the pristine  $\text{V}_2\text{O}_5$ , we compare three experimentally quantities: (i) band gap ( $E_{\text{gap}} = 2.6$  eV), (ii) gap in the conduction band (CB gap = 0.4–0.5 eV), and the number of  $d$  electrons of V ( $N_d = 2.0$ ). While both experimental band gap and CB gap can be obtained using DFT+ $U$ ,  $N_d$  is twice as large as the experimental value, indicating that the  $o$ - $p$ - $V$   $d$  hybridization is overestimated by DFT+ $U$ .



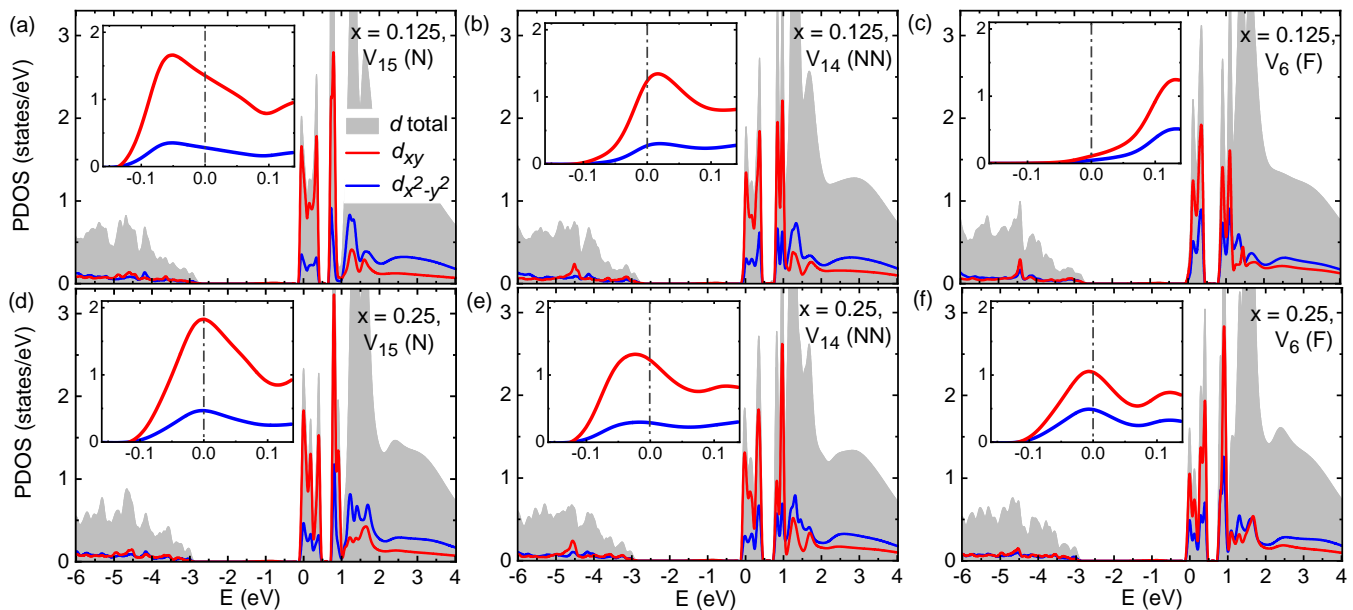


FIG. 9. Projected Density of States (PDOS) onto V  $d$  orbital within DMFT, for (a)-(c)  $\alpha$ -Li<sub>0.125</sub>V<sub>2</sub>O<sub>5</sub> and (d)-(f)  $\alpha$ -Li<sub>0.25</sub>V<sub>2</sub>O<sub>5</sub>. We choose V sites which are nearest neighbor (N) of Li (V<sub>15</sub>), next nearest neighbor (NN) of Li (V<sub>14</sub>), and far (F) from Li ion (V<sub>6</sub>). Here, we use  $U = 5.5$  eV,  $J = 0.5$  eV,  $\lambda = 0.4$  and temperature  $T = 300$  K. Fermi level is set to be zero, and the insets zoom in the region near the Fermi level. This figures show the bound polaronic effects in Li-doped V<sub>2</sub>O<sub>5</sub>.

Our DMFT results shows that for the zero double counting correction, the band gap is not very sensitive on  $U$ , and it is much smaller than the experimental value even with  $U = 6.5$  eV. We found that using nonzero double counting term enlarges the band gap and provides experimental value. Since nonzero double counting term suppress the  $p$ - $d$  hybridization, it is important on the band gap of the charge-transfer insulator V<sub>2</sub>O<sub>5</sub>.

The difference between DFT+ $U$  and DMFT results are more dramatic for Li-doped V<sub>2</sub>O<sub>5</sub>. For both Li<sub>0.125</sub>V<sub>2</sub>O<sub>5</sub> and Li<sub>0.25</sub>V<sub>2</sub>O<sub>5</sub> using DFT+ $U$  method, only the free polaron is preferable, i.e., defect levels are formed in the middle of the band gap. The spin-up defect levels are fully occupied by electrons from Li, and the conduction band is empty. Spatially, the electron at the defect level is localized on one vanadium site. Our DMFT results show both types of polarons as ESP and ENDOR suggested [30, 31], and the delocalized polaronic state is energetically more stable than the free one. In this state, the doped electrons are localized mostly over four Vanadium sites. Thus, the defect level is empty and hidden in the

conduction band, and the electron is occupying at the split-off band, resulting in the increase of the conduction band. The Fermi level shift with Li doping is consistent with recently observed Burstein-Moss shift, which is absorption energy shifts to higher energies, from the optical absorption and photoemission spectroscopy [6, 25].

## V. ACKNOWLEDGEMENT

This work was supported by the Assistant Secretary for Energy Efficiency and Renewable Energy, Office of Vehicle Technologies of the US Department of Energy, through the Battery Materials Research (BMR) program. We also acknowledge financial support from the US Department of Energy, Office of Science, Office of Basic Energy Sciences, Materials Science and Engineering Division. We gratefully acknowledge the computing resources provided on Bebop, a high-performance computing cluster operated by the Laboratory Computing Resource Center at Argonne National Laboratory.

- 
- [1] P. Hu, P. Hu, T. D. Vu, M. Li, S. Wang, Y. Ke, X. Zeng, L. Mai, and Y. Long, Vanadium oxide: Phase diagrams, structures, synthesis, and applications, *Chem. Rev.* **123**, 4353 (2023).
- [2] P. Flowers, K. Theopold, and R. Langley, *Chemistry* (Open Stax, 2015).
- [3] O. Šípr, A. Šimůnek, S. Bocharov, T. Kirchner, and G. Dräger, Geometric and electronic structure effects in polarized V K-edge absorption near-edge structure spectra of V<sub>2</sub>O<sub>5</sub>, *Phys. Rev. B* **60**, 14115 (1999).
- [4] S. Shin, S. Suga, M. Taniguchi, M. Fujisawa, H. Kanzaki, A. Fujimori, H. Daimon, Y. Ueda, K. Kosuge, and S. Kachi, Vacuum-ultraviolet reflectance and photoemission study of the metal-insulator phase transitions in VO<sub>2</sub>, V<sub>6</sub>O<sub>13</sub>, and V<sub>2</sub>O<sub>3</sub>, *Phys. Rev. B* **41**, 4993 (1990).
- [5] G. A. Horrocks, E. J. Braham, Y. Liang, L. R. D. Jesus, J. Jude, J. M. Velázquez, D. Prendergast, and S. Banerjee, Vanadium K-edge X-ray absorption spectroscopy as a probe of the heterogeneous lithiation of V<sub>2</sub>O<sub>5</sub>: First-principles modeling and

- principal component analysis, *J. Phys. Chem. C* **120**, 23922 (2016).
- [6] Q. Wang, M. Brier, S. Joshi, A. Puntambekar, and V. Chakrapani, Defect-induced Burstein-Moss shift in reduced  $V_2O_5$  nanostructures, *Phys. Rev. B* **94**, 245305 (2016).
- [7] J. Meyer, K. Zilberberg, T. Riedl, and A. Kahn, Electronic structure of vanadium pentoxide: An efficient hole injector for organic electronic materials, *J. Appl. Phys.* **110**, 033710 (2011).
- [8] G. L. Simard, J. F. Steger, R. J. Arnott, and L. A. Siegel, Vanadium oxides as oxidation catalysts, *Indust. & Eng. Chem.* **47**, 1424 (1955).
- [9] C. Ruan, X. Wang, C. Wang, L. Zheng, L. Li, J. Lin, X. Liu, F. Li, and X. Wang, Selective catalytic oxidation of ammonia to nitric oxide via chemical looping, *Nature Commun.* **13**, 718 (2022).
- [10] M. S. Whittingham, The role of ternary phases in cathode reactions, *J. Electrochem. Soc.* **123**, 315 (1976).
- [11] S. H. Lim, D. H. Kim, J. Y. Byun, B. K. Kim, and W. Y. Yoon, Electrochemical and catalytic properties of  $V_2O_5/Al_2O_3$  in rechargeable  $LiO_2$  batteries, *Electrochimica Acta* **107**, 681 (2013).
- [12] L. R. D. Jesus, G. A. Horrocks, A. Parija, C. Jaye, L. Wangoh, J. Wang, D. A. Fischer, L. F. Piper, D. Prendergast, and S. Banerjee, Mapping polaronic states and lithiation gradients in individual  $V_2O_5$  nanowires, *Nature Commun.* **7**, 12022 (2016).
- [13] M. B. Smirnov, E. M. Roginskii, K. S. Smirnov, R. Baddour-Hadjean, and J.-P. Pereira-Ramos, Unraveling the structure-raman spectra relationships in  $V_2O_5$  polymorphs via a comprehensive experimental and DFT study, *Inorg. Chem.* **57**, 9190 (2018).
- [14] B. Singh, M. K. Gupta, S. K. Mishra, R. Mittal, P. U. Sastry, S. Rols, and S. L. Chaplot, Anomalous lattice behavior of vanadium pentaoxide ( $V_2O_5$ ): X-ray diffraction, inelastic neutron scattering and ab initio lattice dynamics, *Phys. Chem. Chem. Phys.* **19**, 17967 (2017).
- [15] E. Londero and E. Schröder, Vanadium pentoxide ( $V_2O_5$ ): A van der waals density functional study, *Comput. Phys. Commun.* **182**, 1805 (2011), computer Physics Communications Special Edition for Conference on Computational Physics Trondheim, Norway, June 23-26, 2010.
- [16] E. Londero and E. Schröder, Role of van der waals bonding in the layered oxide  $V_2O_5$ : First-principles density-functional calculations, *Phys. Rev. B* **82**, 054116 (2010).
- [17] S. Sucharitakul, G. Ye, W. R. L. Lambrecht, C. Bhandari, A. Gross, R. He, H. Poelman, and X. P. A. Gao,  $V_2O_5$ : A 2D van der waals oxide with strong in-plane electrical and optical anisotropy, *ACS Appl. Mater. & Inter.* **9**, 23949 (2017).
- [18] N. Kenny, C. Kannewurf, and D. Whitmore, Optical absorption coefficients of vanadium pentoxide single crystals, *J. Phys. Chem. Solid* **27**, 1237 (1966).
- [19] C. Songhee, S. Jaeseok, O. Junhyeob, L. Ji-Hyun, J. J. Hyuck, and L. Shinbuhm, Sharp contrast in the electrical and optical properties of vanadium Wadsley ( $V_mO_{2m+1}$ ,  $m > 1$ ) epitaxial films selectively stabilized on (111)-oriented Y-stabilized  $ZrO_2$ , *Phys. Rev. Mater.* **3**, 063401 (2019).
- [20] A. Othonos, C. Christofides, and M. Zervos, Ultrafast transient spectroscopy and photoluminescence properties of  $V_2O_5$  nanowires, *Appl. Phys. Lett.* **103**, 133112 (2013).
- [21] Q.-H. Wu, A. Thissen, W. Jaegermann, M. Schütz, and P. Schmidt, Resonant photoemission spectroscopy study of electronic structure of  $V_2O_5$ , *Chem. Phys. Lett.* **430**, 309 (2006).
- [22] R. J. O. Mossaneck, A. Mocellin, M. Abbate, B. G. Searle, P. T. Fonseca, and E. Morikawa, Cluster model and band structure calculations of  $V_2O_5$ : Reduced  $V^{5+}$  symmetry and many-body effects, *Phys. Rev. B* **77**, 075118 (2008).
- [23] D. O. Scanlon, A. Walsh, B. J. Morgan, and G. W. Watson, An ab initio study of reduction of  $V_2O_5$  through the formation of oxygen vacancies and li intercalation, *J. Phys. Chem. C* **112**, 9903 (2008).
- [24] E. M. Roginskii, M. B. Smirnov, K. S. Smirnov, R. Baddour-Hadjean, J.-P. Pereira-Ramos, A. N. Smirnov, and V. Y. Davydov, A computational and spectroscopic study of the electronic structure of  $V_2O_5$ -based cathode materials, *J. Phys. Chem. C* **125**, 5848 (2021).
- [25] A. Jarry, M. Walker, S. Theodoru, L. J. Brillson, and G. W. Rubloff, Elucidating structural transformations in  $Li_xV_2O_5$  electrochromic thin films by multimodal spectroscopies, *Chem. Mater.* **32**, 7226 (2020).
- [26] X. Liu, J. Zeng, H. Yang, K. Zhou, and D. Pan,  $V_2O_5$ -based nanomaterials: synthesis and their applications, *RSC Adv.* **8**, 4014 (2018).
- [27] J. M. Cocciantelli, J. P. Doumerc, M. Pouchard, M. Broussely, and J. Labat, Crystal chemistry of electrochemically inserted  $Li_xV_2O_5$ , *J. Power Sources* **34**, 103 (1991).
- [28] D. W. Murphy, P. A. Christian, F. J. DiSalvo, and J. V. Waszczak, Lithium incorporation by vanadium pentoxide, *Inorg. Chem.* **18**, 2800 (1979).
- [29] R. Baddour-Hadjean, E. Raekelboom, and J. P. Pereira-Ramos, New structural characterization of the  $Li_xV_2O_5$  system provided by raman spectroscopy, *Chem. Mater.* **18**, 3548 (2006).
- [30] C. Sanchez, M. Henry, R. Morineau, and M. C. Leroy, Small polaron mobility in  $\alpha$ - $LiV_2O_5$ , *Phys. State Solid (b)* **122**, 175 (1984).
- [31] B. Pecquenard, D. Gourier, and D. Caurant, Electron nuclear double resonance of polarons in  $\alpha$ - $Li_xV_2O_5$ , *J. Phys. Chem.* **100**, 9152 (1996).
- [32] P. Wathaisong, S. Jungthawan, P. Hirunsit, and S. Suthirakun, Transport properties of electron polarons in a  $V_2O_5$  cathode of li-ion batteries: a computational study, *RSC Adv.* **9**, 19483 (2019).
- [33] S. Suthirakun, A. Genest, and N. Rösch, Modeling polaron-coupled Li cation diffusion in  $V_2O_5$  cathode material, *J. Phys. Chem. C* **122**, 150 (2018).
- [34] A. I. Liechtenstein, V. I. Anisimov, and J. Zaanen, Density-functional theory and strong interactions: Orbital ordering in Mott-Hubbard insulators, *Phys. Rev. B* **52**, R5467 (1995).
- [35] G. Kresse and J. Furthmüller, Efficient iterative schemes for ab initio total-energy calculations using a plane-wave basis set, *Phys. Rev. B* **54**, 11169 (1996).
- [36] G. Kresse and J. Hafner, Ab initio molecular-dynamics simulation of the liquid-metal-amorphous-semiconductor transition in germanium, *Phys. Rev. B* **49**, 14251 (1994).
- [37] G. Kresse and J. Furthmüller, Efficient iterative schemes for ab initio total-energy calculations using a plane-wave basis set, *Phys. Rev. B* **54**, 11169 (1996).
- [38] J. P. Perdew, K. Burke, and M. Ernzerhof, Generalized gradient approximation made simple, *Phys. Rev. Lett.* **77**, 3865 (1996).
- [39] S. Grimme, Semiempirical GGA-type density functional constructed with a long-range dispersion correction, *J. Comput. Chem.* **27**, 1787 (2006).
- [40] S. Grimme, A. Hansen, J. G. Brandenburg, and C. Bannwarth, Dispersion-corrected mean-field electronic structure methods, *Chem. Rev.* **116**, 5105 (2016).
- [41] A. Talledo and C. G. Granqvist, Electrochromic vanadium-pentoxide-based films: Structural, electrochemical, and optical properties, *J. Appl. Phys.* **77**, 4655 (1995).
- [42] H. Park, R. Nanguneri, and A. T. Ngo, DFT + DMFT study of spin-charge-lattice coupling in covalent  $LaCoO_3$ , *Phys. Rev. B*

- 101, 195125 (2020).
- [43] A. T. Lee, H. Park, and S. Ismail-Beigi, Origin of the orbital polarization of  $\text{Co}^{2+}$  in  $\text{La}_2\text{CoTiO}_6$  and  $(\text{LaCoO}_3)_1 + (\text{LaTiO}_3)_1$ : A DFT+ $U$  and DMFT study, *Phys. Rev. B* **103**, 125105 (2021).
- [44] DMFTwDFT: An open-source code combining dynamical mean field theory with various density functional theory packages, *Comput. Phys. Commun.* **261**, 107778 (2021).
- [45] A. A. Mostofi, J. R. Yates, Y.-S. Lee, I. Souza, D. Vanderbilt, and N. Marzari, Wannier90: A tool for obtaining maximally-localised Wannier functions, *Comput. Phys. Commun.* **178**, 685 (2008).
- [46] A. Georges, G. Kotliar, W. Krauth, and M. J. Rozenberg, Dynamical mean-field theory of strongly correlated fermion systems and the limit of infinite dimensions, *Rev. Mod. Phys.* **68**, 13 (1996).
- [47] K. Haule, Exact double counting in combining the dynamical mean field theory and the density functional theory, *Phys. Rev. Lett.* **115**, 196403 (2015).
- [48] J. C. Slater, Magnetic effects and the Hartree-Fock equation, *Phys. Rev.* **82**, 538 (1951).
- [49] J. Kanamori, Electron Correlation and Ferromagnetism of Transition Metals, *Prog. Theor. Phys.* **30**, 275 (1963).
- [50] A. Georges, L. d. Medici, and J. Mravlje, Strong correlations from Hund’s coupling, *Annu. Rev. Condens. Matter Phys.* **4**, 137 (2013).
- [51] H. Park, A. J. Millis, and C. A. Marianetti, Computing total energies in complex materials using charge self-consistent DFT + DMFT, *Phys. Rev. B* **90**, 235103 (2014).
- [52] V. M. Galitskii and A. B. Migdal, Application of quantum field theory methods to the many body problem, *J. Exptl. Theoret. Phys.* **34**, 139 (1958).
- [53] X. Wang, M. J. Han, L. de’ Medici, H. Park, C. A. Marianetti, and A. J. Millis, Covalency, double-counting, and the metal-insulator phase diagram in transition metal oxides, *Phys. Rev. B* **86**, 195136 (2012).
- [54] M. Jarrell and O. Biham, Dynamical approach to analytic continuation of quantum Monte Carlo data, *Phys. Rev. Lett.* **63**, 2504 (1989).
- [55] V. Eyert and K.-H. Höck, Electronic structure of  $\text{V}_2\text{O}_5$ : Role of octahedral deformations, *Phys. Rev. B* **57**, 12727 (1998).
- [56] T. K. Le, M. Kang, S. W. Han, and S. W. Kim, Highly intense room-temperature photoluminescence in  $\text{V}_2\text{O}_5$  nanospheres, *RSC Adv.* **8**, 41317 (2018).
- [57] A. E. Bocquet, T. Mizokawa, K. Morikawa, A. Fujimori, S. R. Barman, K. Maiti, D. D. Sarma, Y. Tokura, and M. Onoda, Electronic structure of early 3d-transition-metal oxides by analysis of the 2p core-level photoemission spectra, *Phys. Rev. B* **53**, 1161 (1996).
- [58] K. W. Goodman and V. E. Henrich, Assignment of a photoemission feature in the O-2s–O-2p band gaps of  $\text{TiO}_2$  and  $\text{V}_2\text{O}_5$ , *Phys. Rev. B* **50**, 10450 (1994).
- [59] V. A. Ioffe and I. B. Patrino, Comparison of the small-polaron theory with the experimental data of current transport in  $\text{V}_2\text{O}_5$ , *physica status solidi (b)* **40**, 389 (1970).
- [60] H. Giannetta, C. Calaza, D. Lamas, L. Fonseca, and L. Fraigi, Electrical transport properties of  $\text{V}_2\text{O}_5$  thin films obtained by thermal annealing of layers grown by rf magnetron sputtering at room temperature, *Thin Solid Films* **589**, 730 (2015).
- [61] A. D. Becke and K. E. Edgecombe, A simple measure of electron localization in atomic and molecular systems, *J. Chem. Phys.* **92**, 5397 (1990).
- [62] B. Silvi and A. Savin, Classification of chemical bonds based on topological analysis of electron localization functions, *Nature* **371**, 683–686 (1994).

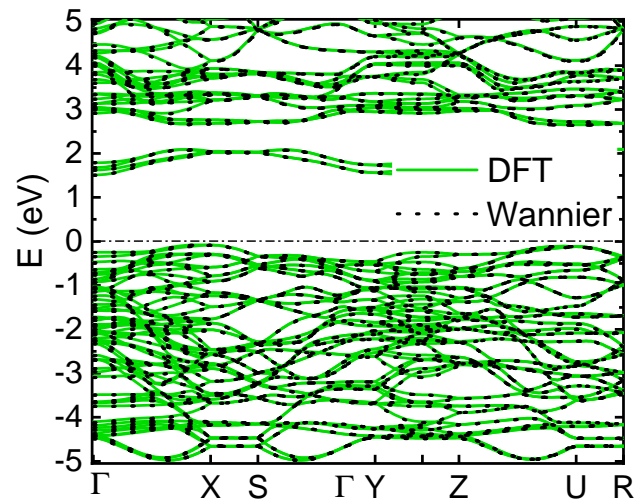


FIG. 10. Band structure calculated by DFT and Wannier function for pristine  $\alpha\text{-V}_2\text{O}_5$ . Fermi level is set at zero.

TABLE VI. Different configuration of  $\text{Li}^+$  ion in supercell 122 using DFT+ $U$ ,  $U = 4$  eV and  $J = 0.0$  eV.

Config.	Change E (eV)	Mom. ( $\mu_B$ )
Center	0.02	1
Off-center	0	1

- [63] A. Ormeci, H. Rosner, F. R. Wagner, M. Kohout, and Y. Grin, Electron localization function in full-potential representation for crystalline materials, *J. Phys. Chem. A* **110**, 1100 (2006).

#### Appendix A: Band structure of pristine $\alpha\text{-V}_2\text{O}_5$

In Figure 10, we compare the DFT and Wannier band structures. This result indicates the plane wave functions fits very well with localized orbital ones.

#### Appendix B: Optimizing Li atom position in $\text{V}_2\text{O}_5$ system

In this appendix, we present our relaxations of  $\text{Li}_x\text{V}_2\text{O}_5$  ( $x = 0.125$  and  $0.25$ ) systems. Several positions of Li atom in  $\text{V}_2\text{O}_5$  framework were checked carefully. With  $x = 0.125$ , a single Li atom was inserted in  $1 \times 2 \times 2$  supercell, (stoichiometric formula of  $\text{Li}_1\text{V}_{16}\text{O}_{40}$ ). First, we inserted a random position of the Li atom [as shown in Figure 11(a)], and after the relaxing process, it moved and located at the middle of the “hole”, which is surrounded by four vanadium atoms (front view). Second, in order to confirm the middle of hole is the most stable position, we adjusted the  $\text{Li}^+$  ion around it. We notify that the position of  $\text{Li}^+$  ion in the off-center gave us a little lower energy of 20 meV than the center. Also, comparing to the previous DFT+ $U$  results about Li-inserted  $\text{V}_2\text{O}_5$  [12, 23], we conclude that the most stable location for  $\text{Li}^+$  ion is the the middle of the hole.

Since the middle of hole is the most stable location for  $\text{Li}^+$  ion, with  $x = 0.25$  case, there are four holes in the supercell.

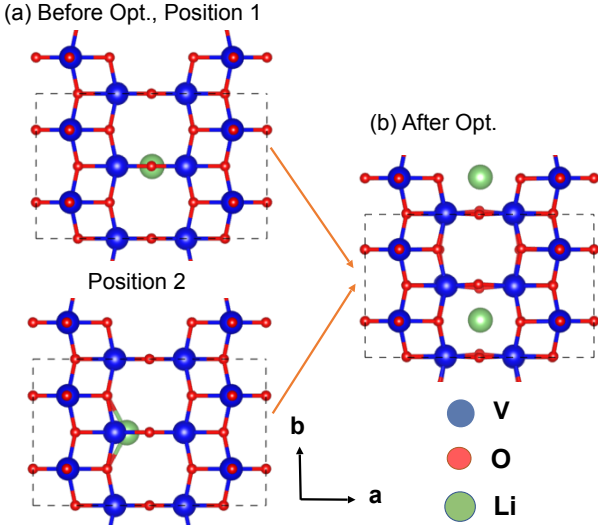


FIG. 11. Atomic structure of  $\text{Li}_{0.125}\text{V}_2\text{O}_5$  (a) before and (b) after optimizations.

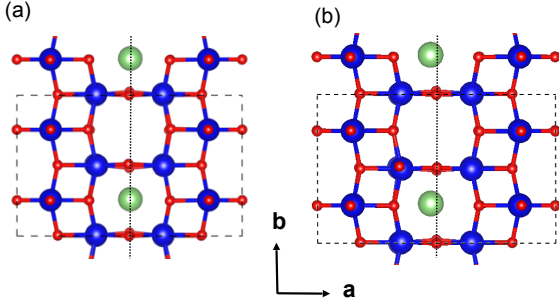


FIG. 12. Atomic structure of  $\text{Li}_{0.125}\text{V}_2\text{O}_5$  for (a)  $\text{Li}^+$  ion at the center of the *hole* and (b)  $\text{Li}^+$  ion at the off-center of the *hole*.

So, we placed the first  $\text{Li}_1^+$  ion in the hole, which is similar to  $x = 0.125$  case, and then chose the second one in the near or far hole [Fig. 13]. As shown in Table VII, we observe that the far-hole situation has lower energy than the near one by 190 meV by minimizing the Coulomb interaction between two  $\text{Li}^+$  ions in the system. We took the far-hole structure for further DMFT study.

TABLE VII. Relative energies of the two different atomic configurations for  $\text{Li}_{0.25}\text{V}_2\text{O}_5$ , with different spin order. Here we used DFT+ $U$  with  $U = 4$  eV and  $J = 0$  eV.

Config.	Energy (eV)	Mag. mom. ( $\mu_B$ )
Near-hole	0.19	2 (FM)
Near-hole	0.19	0 (AFM)
Far-hole	0	2 (FM)

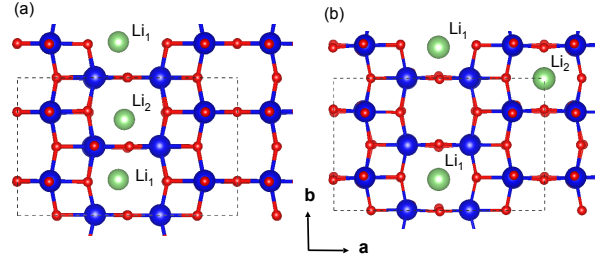


FIG. 13. Atomic structure of  $\text{Li}_{0.25}\text{V}_2\text{O}_5$  for (a) *near-hole* and (b) *far-hole*.

### Appendix C: Testing the free and bound polarons in $\text{Li}_{0.125}\text{V}_2\text{O}_5$ using DFT+ $U$ and DMFT methods

*a. Free polaron:* We used DFT+ $U(=4$  eV)+vdW to optimize the atomic structure. From the optimal structure, we solve non-spin-polarized Kohn-Sham equation using DFT+ $U(=0$  eV)+vdW within VASP. Then, we performed the localized orbital interpolation. Finally, we apply the correlation and hybridization effects within DMFT to the system. By that way, the free polaron was observed by DFT+DMFT. This is a standard procedure for DFT+DMFT calculation, which is described in Refs. [42, 44].

*b. Bound polaron:* There are two reasons which we want to observe the atomic scale existence of the bound polaron. First, experimental measurements including ESR, ENDOR and electronic conductivity suggested the coexistence of free and bound polaron in  $\alpha\text{-Li}_x\text{V}_2\text{O}_5$ . Second, none of the DFT+ $U$  works have predicted about this polaron. However, we have seen that at DFT+ $U(=0$  eV), the doped electron is more delocalizing in the system. So, we altered the standard DFT+DMFT computation as following: (1) From the DFT+ $U(=4$  eV)+vdW structure, we reoptimized it with  $U = 0$  eV with a fixed lattice parameters and non-spin polarized schemes inside VASP. (2) We took this structure for further steps such as wannierisation and self-consistent DMFT calculation. We also test the bound polaronic state in DFT+ $U$  by simply applying  $U = 4$  eV on the optimal DFT as shown in table V.

### Appendix D: Electron localization function

With the optimal structures of  $\text{Li}_x\text{V}_2\text{O}_5$  ( $x = 0$  and  $0.125$ ) obtaining in Sec. II A, we plot their electron localization function (ELF) isosurfaces within DFT+ $U$  using  $U = 4$  eV (as shown in Figure 14). In the nature bond between V and O, we recognize that electrons is localized at O sites, which indicates the ionic bonding [61–63].

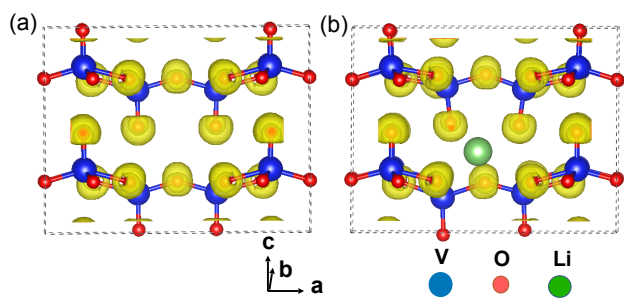


FIG. 14. Isosurface plots of the electron localization function for (a)  $V_2O_5$  and (b)  $Li_{0.125}V_2O_5$ .